Charge density wave transitions, soft phonon, and possible electronic nematicity in $BaNi_2(As_{1-x}P_x)_2$

Christoph Meingast,[1] Anmol Shukla,[1] Liran Wang,[1] Rolf Heid,[1] Frédéric Hardy,[1] Mehdi Frachet,[1] Kristin Willa,[1] Tom Lacmann,[1] Matthieu Le Tacon,[1] Michael Merz,[1,2] Amir-Abbas Haghighirad,[1] and Thomas Wolf[1]

[1]*Institute for Quantum Materials and Technologies, Karlsruhe Institute of Technology, 76021 Karlsruhe, Germany*

[2]*Karlsruhe Nano Micro Facility (KNMFi), Karlsruhe Institute of Technology (KIT), 76344 Eggenstein-Leopoldshafen, Germany*

(Received 8 July 2022; revised 9 September 2022; accepted 3 October 2022; published 19 October 2022)

A detailed investigation of $BaNi_2(As_{1-x}P_x)_2$ single crystals using high-resolution thermal-expansion, heat-capacity, Young's-modulus, and resistivity measurements is presented. The phase diagram of $BaNi_2(As_{1-x}P_x)_2$ is shown to be much richer than suggested by the original data of Kudo *et al.* [Phys. Rev. Lett. **109**, 097002 (2012)]. The transition to the commensurate charge density wave (C-CDW) is always preceded by a fourfold symmetry-breaking transition associated with the long-range ordering of a strongly fluctuating unidirectional incommensurate charge density wave (I-CDW). Significant precursors above the I-CDW and C-CDW transitions are seen in the thermal expansion and resistivity and are particularly evident in the temperature dependence of the c/a ratio of the lattice parameters. Heat-capacity measurements of the crystals with a higher P content and a higher critical temperature of 3.2 K uncover a Debye-like behavior of a soft-phonon mode with a very low Θ_{Debye} of roughly 50 K. Associated with this soft phonon are unusually large thermal-expansion anomalies, resulting in logarithmically diverging uniaxial phonon Grüneisen parameters. Young's-modulus data of these higher-T_c crystals exhibit a significant softening in both B_{1g} and B_{2g} channels, which is argued to be incompatible with nematic criticality and is rather associated with a broad phase transition to an hitherto unknown structure. Possible origins of the increase in the superconducting critical temperature with P substitution are discussed.

DOI: 10.1103/PhysRevB.106.144507

I. INTRODUCTION

$BaNi_2As_2$ crystallizes in the same $ThCr_2Si_2$ structure as $BaFe_2As_2$ [1], and, interestingly, undergoes a structural phase transition to a triclininc phase at a similar temperature (135 K) as the stripe spin density wave (SDW) transition in $BaFe_2As_2$ [2,3]. However, no signatures of magnetism have been found in neutron-diffraction [4], magnetic susceptibility [2], or photoemission [5] studies. Rather, recent diffraction experiments have shown that the triclinic phase is associated with a commensurate charge density wave (C-CDW) order, and that an incommensurate charge density wave (I-CDW) precedes the triclinic transition by a few kelvin [6–9]. Recent high-resolution thermal-expansion data exhibit a clear fourfold symmetry breaking at this I-CDW transition, to an orthorhombic structure with space group *Immm* [9]. Pure $BaNi_2As_2$, in contrast to $BaFe_2As_2$, is already superconducting with a very low critical temperature, T_c, of 0.7 K [2]. T_c can, however, be increased significantly to roughly 3 K by suppressing the triclinic phase transition through various substitutions on all three atomic positions [6,10,11]. In the system $BaNi_2(As_{1-x}P_x)_2$, Kudo *et al.* attributed this increase in T_c to an enhanced electron-phonon coupling due to a soft-phonon mode, although, surprisingly, no increase in the electronic density of states was found [10]. In contrast, Eckberg *et al.* provided evidence for significant B_{1g} nematic fluctuations via elastoresistive measurements in $(Ba,Sr)Ni_2As_2$ and suggested that nematic fluctuations might be the origin of the increased T_c [11]. Theoretically, the phase transitions and superconductivity have been associated with an orbital-selective Peierls instability [12], or orbital fluctuations [13]. Initial density functional theory (DFT) calculations on $BaNi_2As_2$ in the tetragonal $ThCr_2Si_2$ structure by Subedi and Singh [14] classified this material as a conventional phonon-mediated superconductor, in which the strongest electron-phonon coupling was found in the vicinity of low-lying optical phonons. Interestingly, the calculated T_c of 4 K in this study is close to the highest T_c so far obtained by suppressing the triclinic transition by the various substitutions. Several questions emerge from these studies. Is T_c raised by soft phonons or by B_{1g} nematic fluctuations, or, alternatively, is there a close connection between these? Should one even think of an enhanced T_c by these effects, or is it more appropriate to think of a suppressed T_c due to the CDW order and associated distortions in the triclinic phase? What is the nature of the soft phonon and/or nematic fluctuations in these systems, and how are these influenced by various substitutions?

In this paper we take another look at the $BaNi_2(As_{1-x}P_x)_2$ system using detailed high-resolution thermal-expansion, heat-capacity, Young's-modulus, and resistivity measurements. First, the phase diagram of $BaNi_2(As_{1-x}P_x)_2$ is shown to be much richer than suggested by the original data of Kudo *et al.* [10]. In particular, we demonstrate that the triclinic phase is always preceded by a fourfold symmetry-breaking transition, which we attribute to the long-range ordering of the unidirectional I-CDW. Further, crystals with the higher-T_c phase, i.e., in which the triclinic phase is suppressed with P

substitution, surprisingly also exhibit a clear phase transition to an unknown low-temperature structure. Significant precursors above the I-CDW and C-CDW transitions are resolved in thermal-expansion and resistivity data and are particularly evident in the temperature dependence of the c/a ratio of the lattice parameters. The thermal-expansion data allow us to study the temperature evolution of the lattice parameters in the tetragonal $ThCr_2Si_2$ structural setting with P substitution. We find that the largest effect occurs perpendicular to the Ni planes, where the lattice shrinks by roughly 1.5% upon cooling in $BaNi_2As_2$. This c-axis shrinking decreases strongly with increasing P content and, surprisingly, changes sign to a small expansion for the higher-T_c material. Our detailed heat-capacity measurements uncover a Debye-like behavior of the soft-phonon mode with a very low Debye temperature, T_{Debye}, of roughly 50 K.

Associated with this soft phonon are large thermal-expansion anomalies, resulting in large and logarithmically diverging phonon Grüneisen parameters. To check for the expected softening of the shear modulus at a nematic phase transition, Young's-modulus measurements [15] were performed on the higher-T_c phase. A significant softening in both B_{1g} and B_{2g} channels is found, and this is argued not to be compatible with nematic criticality. Detailed resistivity data provide evidence for a dominant electron-electron scattering only in the higher-T_c phase. Finally, we argue that nematic fluctuations are not the main drivers for superconductivity in $BaNi_2(As_{1-x}P_x)_2$, and that the strong-coupling superconductivity in these systems is most likely related to the soft-phonon mode of the CDW transitions.

II. METHODS

Single crystals of $BaNi_2(As_{1-x}P_x)_2$ were grown using a self-flux method, as described in more detail in Refs. [9,16,17]. Electron microprobe analysis of the crystals was performed using a benchtop scanning electron microscope—energy dispersive x-ray spectroscopy (EDS) device COXEM EM-30plus equipped with an Oxford detector (operating with AztecLive software). The EDS analyses on the $BaNi_2(As_{1-x}P_x)_2$ crystals of the present study revealed phosphorus contents $x = 0.035(5)$, $0.048(5)$, $0.075(5)$, and $0.100(5)$.

X-ray diffraction data on representative $BaNi_2(As_{1-x}P_x)_2$ single-crystal samples from the same batches were collected at 295 K on a STOE imaging plate diffraction system (IPDS-2T) using Mo $K\alpha$ radiation. For the investigated specimen all accessible reflections ($\approx$5100) were measured up to a maximum angle of $2\Theta = 65^\circ$. The data were corrected for Lorentz, polarization, extinction, and absorption effects. Using SHELXL [18] and JANA2006 [19], all averaged symmetry-independent reflections ($I > 2\sigma$) have been included for the refinements. For all compositions the unit cell and the space group were determined, the atoms were localized in the unit cell utilizing random phases as well as Patterson superposition methods, the structure was completed and solved using difference Fourier analysis, and finally the structure was refined. In all cases the refinements converged quite well and show excellent reliability factors [see goodness of fit (GOF), R_1, and wR_2 in Table I]. There are several interesting trends in these data. First, the a lattice parameter, the Ni-(As,P) bond length, and the z parameter all exhibit significant reductions with P substitution. Second, the anisotropic displacement parameters (ADPs) change in an interesting and systematic fashion: The ADPs of Ba and (As-P) are very anisotropic for $x = 0$ and become almost isotropic with increasing P content. The ADPs of Ni, on the other hand, are almost isotropic for $x = 0$ and become increasingly anisotropic towards $x = 0.1$. This trend cannot simply be explained by As-P disorder since the equivalent ADPs (i.e., the directional weighted average of the U_{ii}) are not increasing. It rather reflects changes of the orbital degree of freedom, most probably in the way discussed in [9] where it was shown that the contribution of the $3d_{xy}$ ($3d_{xz,yz}$) orbitals on the Ni site is gradually reduced (enhanced) with increasing P substitution. The compositions of the x-ray data are, within the error, consistent with the EDS measurements. In the following we use the EDS values.

Thermal expansion and Young's modulus were measured using a home-built high-resolution capacitance dilatometer [20]. A three-point-bending technique [21] was employed for the Young's modulus determination. Heat-capacity and resistivity measurements were made in a physical property measurement system from Quantum Design. Details of DFT calculations are described in Ref. [22,32].

III. RESULTS

In this section we concentrate on making a detailed comparison between crystals with widely different P contents, i.e., one with a clear triclinic phase transition and a low $T_c = 0.7$ K ($x = 0.048$) and one without the triclinic transition and a higher $T_c = 3.2$ K ($x = 0.10$), using thermal-expansion, heat-capacity, Young's-modulus, and resistivity measurements. With this comparison we hope to shed new light on the CDW transitions, the soft-phonon effects, as well as possible electronic nematicity. Additionally, the complete phase diagram will be mapped out using thermal-expansion measurements on crystals with additional P contents.

A. Thermal expansion: $x = 0.048$

In Fig. 1 the relative length changes, $\Delta L/L_{300\,\text{K}} = [L(T) - L_{300\,\text{K}}]/L_{300\,\text{K}}$, along the tetragonal $[100]_{\text{tet}}$, $[110]_{\text{tet}}$, and $[001]_{\text{tet}}$ directions upon cooling and warming [Fig. 1(a)] are plotted for a crystal with $x = 0.048$, together with the corresponding thermal-expansion coefficients, $\alpha = (1/L)(dL/dT)$, upon warming [Fig. 1(b)]. Clearly observed are both the transitions (upon cooling and heating) to the orthorhombic phase discussed in [9] at $T_{\text{orth}} = 106$ K and to the triclinic phase at $T_{\text{tric}} = 80$ K [3,6–9,11]. The discontinuous change in lengths and the large thermal hysteresis at T_{tric} are consistent with the strong first-order character of the triclinic transition. Hereafter, we will continue to use the tetragonal notation for the triclinic phase, since it is impossible to reorient the crystal along the triclinic axes in the dilatometer. Thus, although the thermal expansion below T_{tric} does not correspond to the triclinic crystallographic directions, this, as will be shown, provides very useful information about the general structural evolution with temperature for different P substitutions. Moreover, the triclinic distortion is quite small with respect to the

TABLE I. Crystallographic data for $BaNi_2(As_{1-x}P_x)_2$ at 295 K determined from single-crystal x-ray diffraction. The structure was refined in the tetragonal space group (SG) $I4/mmm$ for which the lattice parameters a and c are shown together with the volume V of the unit cell. Ba sits on a $2a$ Wyckoff position with coordinates 0, 0, 0; Ni on a $4d$ position with coordinates $\frac{1}{2}$, 0, $\frac{1}{4}$; and (As,P) on a $4e$ position with coordinates 0, 0, z. The U_{ii} denote the anisotropic atomic displacement parameters (for all these special positions $U_{11} = U_{22}$ and $U_{12} = U_{13} = U_{23} = 0$). For completeness the bond distances for Ba-(As,P), Ni-(As,P), and (As,P)-(As,P) along the crystallographic c direction are depicted as well. The refinements for $x = 0$ and $x = 3\%$ are reproduced from Ref. [9]. Errors shown are statistical errors from the refinement.

x (%)	0	3.0(8)	3.3(7)	4.2(10)	6.0(7)	7.1(4)	10.2(5)
a (Å)	4.1413(6)	4.1358(8)	4.1379(4)	4.1401(5)	4.1353(5)	4.1327(5)	4.1286(8)
c (Å)	11.6424(24)	11.6468(35)	11.6432(15)	11.6421(20)	11.6415(22)	11.6397(18)	11.6375(32)
V (Å^3)	199.7	199.2	199.4	199.6	199.1	198.8	198.4
			Ba, $2a$: 0, 0, 0				
U_{11} (Å^2)	0.01256(39)	0.01104(32)	0.01015(19)	0.01262(57)	0.01248(40)	0.01123(14)	0.01164(16)
U_{33} (Å^2)	0.02001(48)	0.01802(42)	0.01819(32)	0.01735(61)	0.01347(45)	0.01173(15)	0.01125(17)
			Ni, $4d$: $\frac{1}{2}$, 0, $\frac{1}{4}$				
U_{11} (Å^2)	0.02106(64)	0.01955(44)	0.01937(28)	0.02421(69)	0.02111(49)	0.02094(20)	0.02134(23)
U_{33} (Å^2)	0.02216(71)	0.02177(59)	0.02247(48)	0.01689(75)	0.01633(63)	0.01402(21)	0.01379(23)
			(As,P), $4e$: 0, 0, z				
z	0.34727(10)	0.34704(9)	0.34703(6)	0.34696(11)	0.34688(9)	0.34677(4)	0.34665(5)
U_{11} (Å^2)	0.01539(42)	0.01357(45)	0.01310(27)	0.01753(69)	0.01492(48)	0.01407(19)	0.01425(22)
U_{33} (Å^2)	0.02638(65)	0.02501(65)	0.02618(33)	0.02175(98)	0.01839(76)	0.01839(25)	0.01725(28)
			Selected bond lengths				
Ba-(As,P) (Å)	3.4258(16)	3.4243(15)	3.4254(14)	3.4258(15)	3.4246(8)	3.4235(6)	3.4216(9)
Ni-(As,P) (Å)	2.3601(16)	2.3566(15)	2.3573(13)	2.3589(14)	2.3552(7)	2.3534(5)	2.3508(8)
(As,P)-(As,P) (Å)	3.5691(10)	3.5630(11)	3.5652(16)	3.5587(16)	3.5651(8)	3.5670(8)	3.5692(10)
			Goodness of fit and R values				
GOF	2.33	2.17	1.68	1.18	1.45	0.75	1.27
wR_2 (%)	5.07	4.59	3.58	4.30	3.94	1.98	2.83
R_1 (%)	1.94	1.83	1.53	1.92	1.63	0.93	1.21

tetragonal room-temperature structure [3,6–11]. That is, when the triclinic structure is projected onto a slightly distorted tetragonal one (based on the corresponding small shifts of the atoms in the low-temperature phase with respect to their position in the high-temperature tetragonal cell), the lattice parameters and angles are as follows: $a = 4.1504$ Å, $b = 4.1538$ Å, $c = 11.5169$ Å and $\alpha = 89.91^\circ$, $\beta = 89.92^\circ$, $\gamma = 90.03^\circ$. The largest thermal-expansion effect occurs along the $[001]_{tet}$ direction, i.e., perpendicular to the NiAs planes, where the lattice shrinks by about 0.85% upon cooling. This shrinking is not restricted to the triclinic phase transition itself, but already starts significantly above T_{tric}, as clearly demonstrated by the expansivity in Fig. 1(b). Here we can identify two related temperatures: (1) T_{cross} where the in-plane and out-of-plane thermal-expansion coefficients cross and (2) T_{fluct} which marks the onset of the transition, i.e., where the expansivities start to deviate from a more regular temperature dependence. This behavior is mirrored nicely in the c/a ratio shown in Fig. 1(c), calculated using room-temperature values of the lattice parameters from Refs. [9,10]. Since the expansivity at high temperatures along $[001]_{tet}$ is much smaller than along $[100]_{tet}$, the c/a ratio increases with decreasing temperatures until reaching a maximum at T_{cross} and then decreases sharply at the triclinic transition. The temperatures T_{fluct}, T_{cross}, T_{orth}, and T_{tric} will later be used for mapping out the phase diagram. It is also worth noting that the expansivity at 300 K is already anomalous, since $\alpha_{[\,001\,]}$ is much smaller than $\alpha_{[\,100\,]}$ [see Fig. 1(b)]. This is opposite of what is found for $BaFe_2As_2$ [23] and is an indication for additional physics besides the normal anharmonic phonon-induced thermal expansion operating already in the high-temperature tetragonal phase.

B. Fourfold symmetry-breaking transition at T_{orth}: $x = 0.048$

As demonstrated previously [9,24–26], an orthorhombic distortion can be detected in a capacitance dilatometer by measuring the expansion along two different in-plane directions due to the detwinning effect of the small uniaxial pressure applied by the device. In Fig. 1(a), a clear splitting of the thermal expansion along the $[100]_{tet}$ and $[110]_{tet}$ directions is observed below T_{orth}, marking the onset of in-plane symmetry breaking. Here the "detwinning" effect occurs for pressure applied along the $[100]_{tet}$ direction, suggesting a transition to an orthorhombic structure with space group $Immm$ [9]. Together the $[100]_{tet}$ and $[110]_{tet}$ data sets allow (under the assumption that the uniaxial pressure applied by the dilatometer is large enough to fully detwin the crystal) to calculate the orthorhombic distortion $\delta = (a - b)/(a + b)$ [see Fig. 2(a)]. Note that the orthorhombic distortion in $BaFe_2As_2$ is significantly larger and occurs along the $[110]_{tet}$ instead of the $[100]_{tet}$ direction in the Ni compound [27]. In Fig. 2(b) the derivative of δ is plotted together with heat-capacity data, for which a straight line has been subtracted in order to make the tiny anomaly, which is only about $\Delta C_p/T = 4$ mJ/(mole K^2), visible. Both quantities exhibit a sharp peak at $T_{orth} = 106$ K.

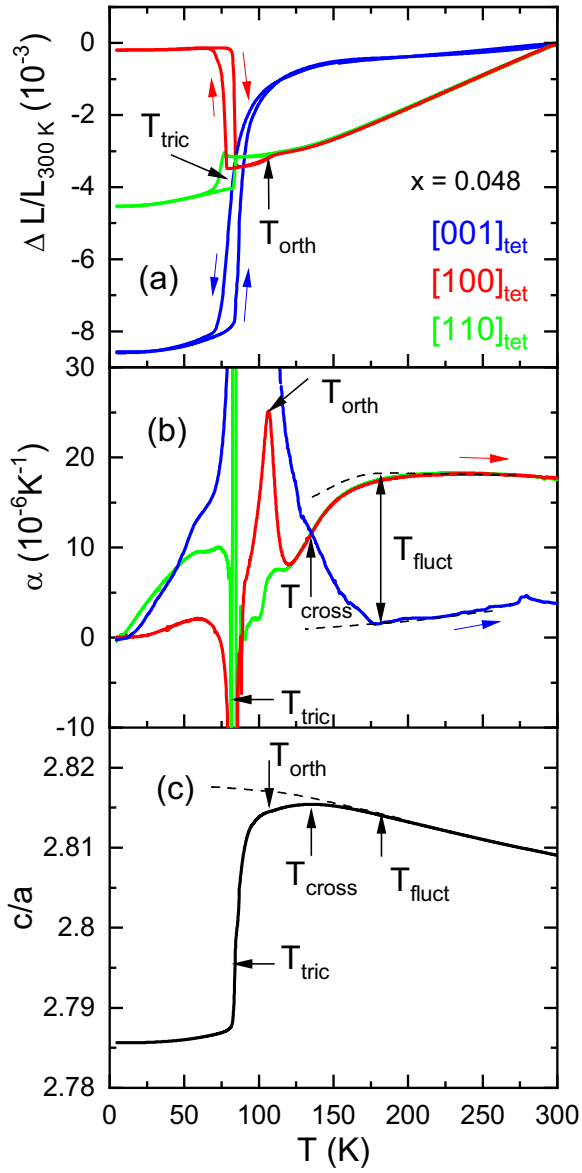

FIG. 1. (a) Relative thermal expansion, $\Delta L/L_{300\,\mathrm{K}}$, (b) thermal-expansion coefficient, $\alpha = (1/L)(dL/dT)$, and (c) c/a ratio of the lattice parameters for $x = 0.048$. Clearly visible are the fourfold symmetry-breaking transition at T_{orth} and the triclinic transition at T_{tric}. Significant precursors to these transitions are seen in the c/a ratio and are marked by their onset, T_{fluct}, and T_{cross}, where α_a and α_c cross leading to the maximum in c/a. The colored arrows indicate cooling and heating curves (see text for details).

This behavior is reminiscent of a strongly fluctuating low-dimensional transition, in contrast to the very mean-field-like behavior in Fe-based nematic transitions [15,25,28,29]. Surprisingly, no clear feature is seen in the in-plane resistivity at T_{orth} (note, here a straight line has been subtracted to highlight the anomaly)—rather a very broad increase in the resistivity starting at roughly 150 K is observed, which suggests a correlation of the resistivity anomaly with T_{fluct} and T_{cross} instead of T_{orth}. This interpretation is also supported by the resistivity data for $x = 0.10$ (see Fig. 9 and other detailed resistivity measurements in Ref. [17]).

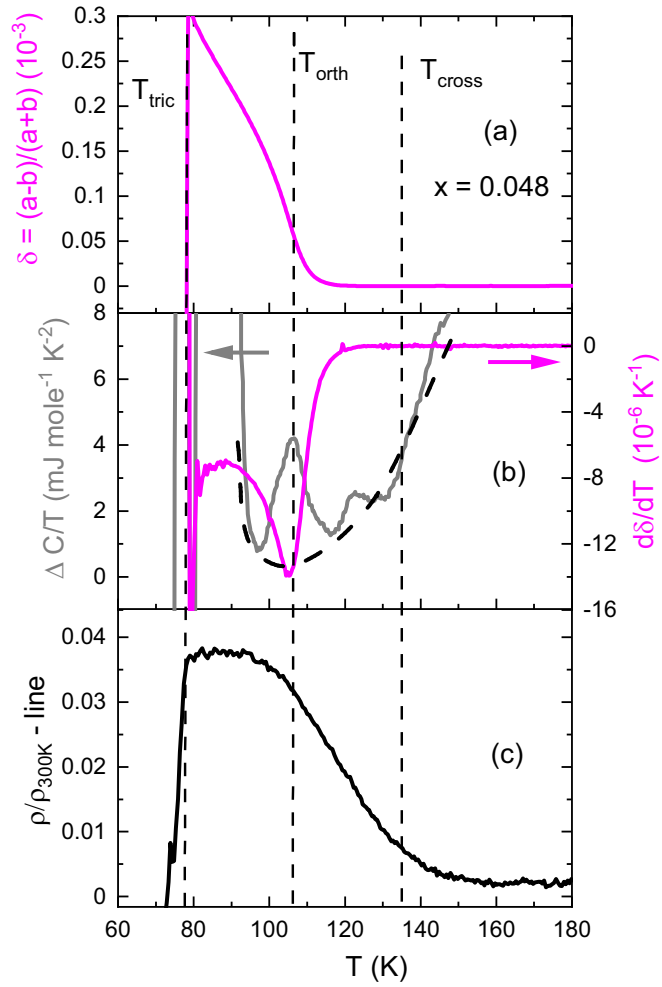

FIG. 2. Temperature dependence of (a) orthorhombic distortion, δ, (b) heat capacity and $d\delta/dT$ and (c) in-plane resistivity, $\Delta\rho/\rho_{300\,\mathrm{K}}$ around T_{orth} for $x = 0.048$. Whereas clear anomalies are observed in both ΔC_p and $d\delta/dT$, no clear anomaly is seen in the resistivity. Linear backgrounds have been subtracted from both heat-capacity and resistivity data. The curved dashed black line in (b) represents an approximate background to the heat-capacity anomaly (see text for details).

C. Thermal expansion $x = 0.10$: Evidence for an additional phase transition

Next we turn to the thermal expansion of the crystal with $x = 0.10$, which is not expected to exhibit a triclinic transition [10]. Surprisingly, clear signs of a phase transition of unknown origin for this composition are observed in the thermal expansion. In particular, the thermal expansion along the $[001]_{\mathrm{tet}}$ direction exhibits an expansion upon cooling at a strongly hysteretic transition at $T_x = 50$ K [see Fig. 3(a)]. This expansion counteracts the contraction due to high-temperature fluctuations, such that the total relative length change along the c axis from 300 to 5 K is nearly zero. In contrast, the transition at T_x has only a very small effect upon the in-plane lengths, and is made only visible in the $[100]_{\mathrm{tet}}$ expansion coefficients [see Fig. 3(b)]. We see no sign of the orthorhombic transition, at which one would expect a positive signal in α_{100} [see Fig. 1(b)] due to the detwinning effect

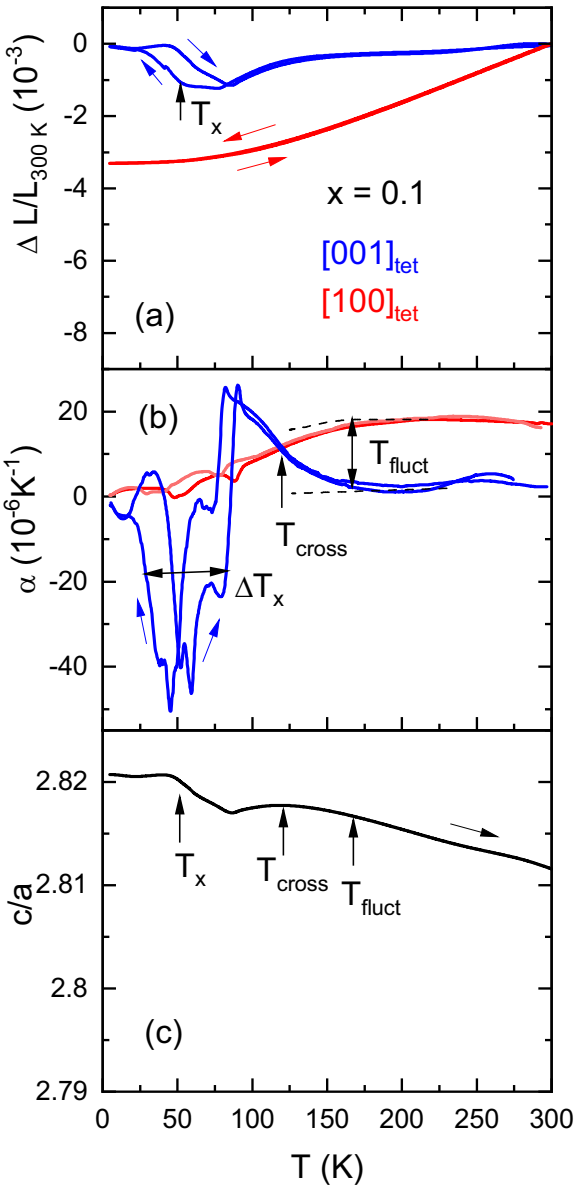

FIG. 3. (a) Relative uniaxial thermal expansion, $\Delta L/L_{300\,\mathrm{K}}$, (b) thermal-expansion coefficients, α_{100} and α_{001}, and (c) c/a ratio of the lattice parameters for $x = 0.10$. Clearly visible along the $[001]_{\mathrm{tet}}$ direction is a first-order phase transition at T_x to a hitherto unknown structure. The colored arrows indicate cooling and heating curves. In contrast to the c/a ratio for $x = 0.048$, c/a does not exhibit a large reduction upon cooling (see text for details).

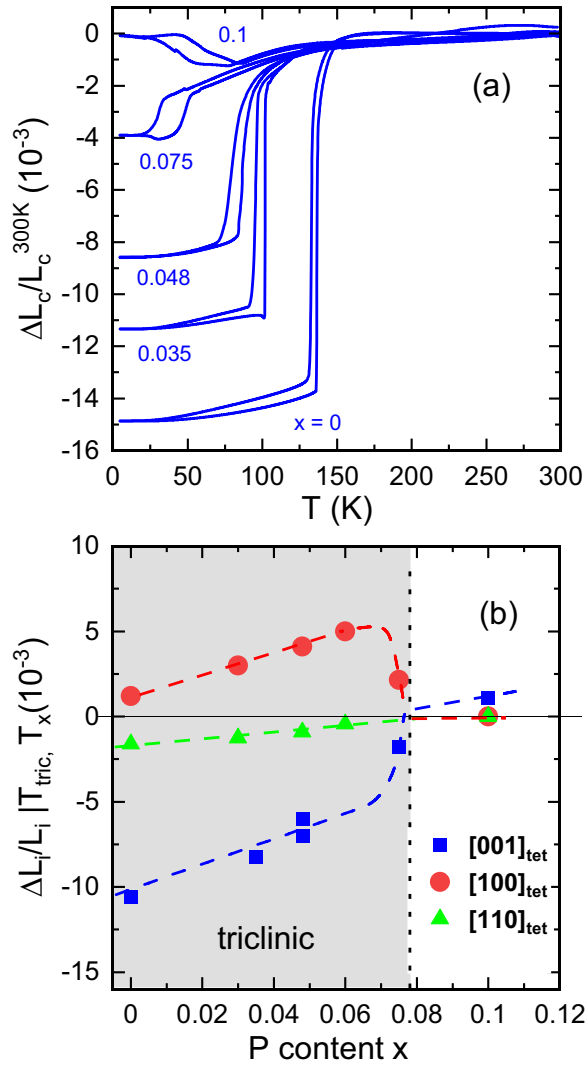

FIG. 4. (a) Temperature dependence of the relative thermal expansion along $[001]_{\mathrm{tet}}$, demonstrating the suppression of the c-axis contraction and the sign change upon P substitution. (b) P-content dependence of the discontinuous relative length changes at the first-order transitions T_{tric} and T_x along all three tetragonal directions. (see text for details).

of the dilatometer, which always measures the shorter of the two orthorhombic axes. Instead, α_{100} drops slightly at the onset at T_x [see red lines in Fig. 3(b)] and also exhibits a significant hysteresis. Both of these findings are inconsistent with the second-order orthorhombic transition seen in all other P concentrations [9]. Possible origins of this transition will be discussed further on. At higher temperatures we can again identify both T_{cross} and T_{fluct} as in the crystals with lower P content. Both of these temperatures are slightly reduced in comparison to those found for $x = 0.048$.

D. *c*-axis thermal expansion and structural evolution with P substitution

The evolution of the c-axis thermal expansion for several additional P substitutions is shown in Fig. 4. The magnitude of the c-axis contraction upon cooling is drastically reduced with increasing P content and changes sign to a small expansion for $x = 0.10$. The opposite sign of the transition for $x = 0.10$, as well as the fact that it occurs at a higher temperature than the triclinic transition for $x = 0.075$, strongly imply that this is not due to an inhomogeneous crystal with a remaining fraction of the triclinic phase, but rather to a new phase. The P dependence of the discontinuous length changes along all three measured directions at the first-order transitions at T_{tric} and T_x (for $x = 0.10$) are presented in Fig. 4(b). Whereas the magnitude of the shrinking along $[001]_{\mathrm{tet}}$ decreases with increasing x, the expansion along

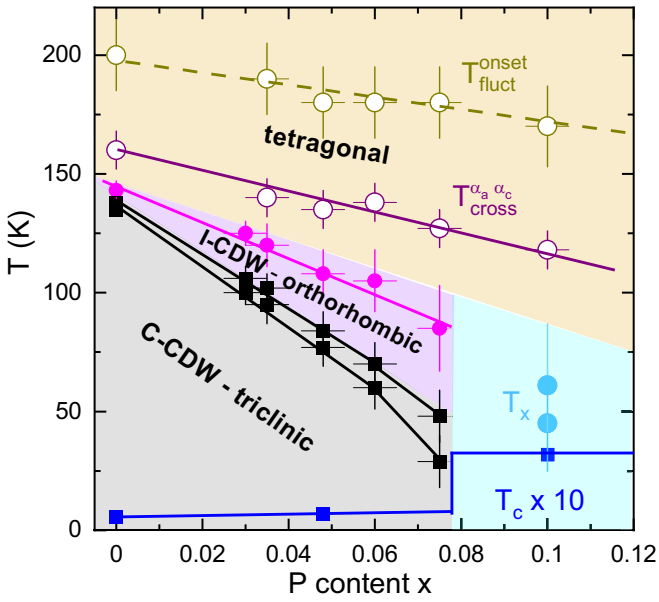

FIG. 5. Phase diagram of $BaNi_2(As_{1-x}P_x)_2$ determined from thermal-expansion and heat-capacity data. Closed symbols represent real thermodynamic phase transitions, and open symbols represent crossover temperatures. T_{fluc} and T_{cross} decrease monotonically across the whole doping range. In contrast, T_{orth} and T_{tric} disappear near $x = 0.08$ and are replaced by the transition at T_x, leading to the higher superconducting T_c. The thermal hysteresis for cooling and heating at T_{tric} and T_x is indicated by double symbols. The steplike increase of T_c is based on the results from [10] (see text for details).

$[100]_{tet}$ increases with x until about $x = 0.075$, beyond which all effects are abruptly reduced in magnitude. This highlights the first-order nature of the vanishing triclinic phase with P substitution.

E. Phase diagram

The thermal-expansion data allows us to construct a detailed phase diagram showing the evolution of T_{fluct}, T_{cross}, T_{orth}, and T_{tric} with P substitution, as well as the newly discovered transition at T_x (see Fig. 5). T_{fluc} and T_{cross} decrease slightly with x and are visible over the entire range of x studied, suggesting that the fluctuations at high temperature are present over this whole substitution region. On the other hand, T_{orth} and T_{tric} decrease significantly faster and are only observed up to $x = 0.075$. The higher T_c occurs only in the higher substitution region (i.e., $x > 0.075$), as detailed by the original work of Kudo *et al.* [10]. The x dependence of T_{orth}, the high-temperature fluctuations characterized by T_{fluct} and T_{cross}, as well as the transition at T_x are new findings, which were previously [10] not recognized in the phase diagram of $BaNi_2(As_{1-x}P_x)_2$.

F. Heat capacity for $x = 0.048$ and $x = 0.10$: Temperature evolution of soft-phonon contribution

In the following we further analyze our data in order to gain a better understanding of the soft phonon and the large increase of T_c from pure $BaNi_2As_2$ to crystals with $x = 0.10$. A comparison of the heat capacity of crystals with $x = 0.048$ and $x = 0.10$ are shown in Fig. 6(a) in a C_p/T vs T^2 representation. As observed previously [10], the crystal with the higher T_c exhibits a much larger slope, i.e., Debye contribution, suggesting a significant lattice softening. On the other hand, the Sommerfeld coefficient, γ, is surprisingly independent of the P content, in agreement with Ref. [10]. The coupling strength, $\Delta C_p/\gamma T_c$, increases from a weak-coupling value of 1.4 to

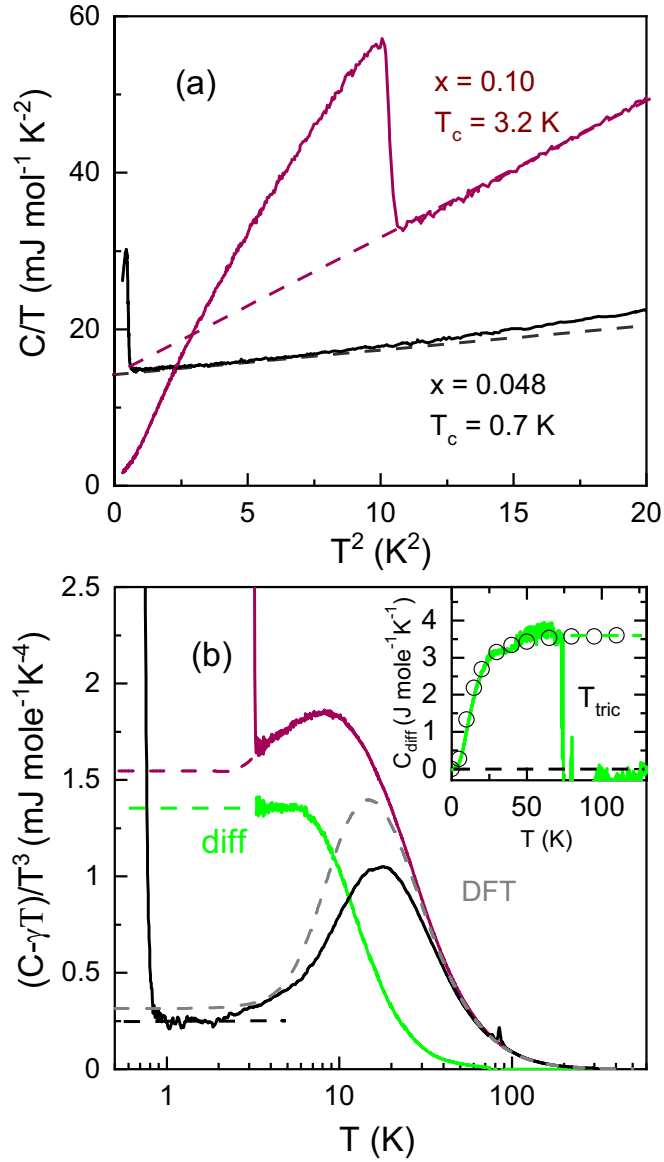

FIG. 6. (a) Heat capacity C/T versus T^2 for $x = 0.048$ and 0.10. Dashed lines are linear fits demonstrating the increase in the phonon Debye term with increasing P content, as well as the P-content independent electronic γ. (b) Phonon heat capacity divided by T^3. Here, the low-T constant value is indicative of Debye behavior due to acoustic phonons, and the peaks near 10–20 K result from optical phonons. The difference between $x = 0.10$ and $x = 0.048$ (green curve) is reminiscent of a Debye-like heat capacity with a very low $\theta_{Debye} = 10$–15 K and disappears above the triclinic transition (see inset). The open circles in the inset represent a Debye heat capacity with $\theta_{Debye} = 50$ K. Heat capacity from DFT calculations in the stable tetragonal state for $x = 0$ (dashed gray curve) is very similar to the experimental data for $x = 0.048$.

a strong-coupling value of 2.0 for $x = 0.048$ and $x = 0.10$, respectively, consistent with Ref. [10]. The significance of this tendency to strong coupling will be discussed later. By subtracting the electronic term γT from C_p and plotting the resulting phonon heat capacity divided by T^3 vs $\log T$, we can obtain more detailed information about the evolution of the anomalous Debye (T^3) term [see Fig. 6(b)]. In this representation, a Debye heat capacity gives a constant C_{phonon}/T^3 term well below the Debye temperature, T_{Debye}, and then smoothly approaches zero at higher temperatures. A peak, on the other hand, is indicative of optical phonons, which can be represented by Einstein heat capacities (see, e.g., Ref. [30]). The expected Debye behavior for the $x = 0.048$ crystal is clearly seen at very low T (between 0.7 and 2.5 K), and low-lying optical phonons give rise to the peak centered at roughly 20 K. For the $x = 0.10$ crystal, C_{phonon}/T^3 is significantly larger at low T, but never really reaches a constant value before entering the superconducting state at 3.2 K. The difference between these curves (green curve) suggests that the large phonon softening observed in the $x = 0.10$ composition arises from a Debye-like term with a low T_{Debye} of approximately 50 K, as illustrated in the inset of Fig. 6(b) by the open circles. Rather than originating from acoustic phonons, we suggest that this softening is associated with the soft optical phonon recently observed by Raman and inelastic x-ray investigations [16,31,32]. This softening, which is located at the I-CDW wave vector, extends to zero energy at temperatures already significantly above the triclinic transition in $BaNi_2As_2$. Here, we assume that this phonon softening extends down to low temperature in the $x = 0.10$ crystal, which has no triclinic transition, and that the heat capacity associated with this softening may, thus, mimic a Debye-like term. The relative weight of this Debye term [3.5 J/(mole K)] amounts to only roughly 3% of the Dulong-Petit value, demonstrating that only a fraction of a single-phonon branch is affected by this softening. Further, we observe that the difference in heat capacity abruptly vanishes above $T_{\text{tric}} = 80$ K [see inset in Fig. 6(b)]. This suggests that the same phonon softening is present also in the $x = 0.048$ crystal above, but not below, T_{tric}.

The phonon heat capacity from our DFT calculations in the tetragonal structure [gray dashed curve in Fig. 6(b)] roughly matches data for the triclinic phase ($x = 0.048$) both in the location of the optical phonon peak and the value of the Debye term. In these calculations, the $E_{g,1}$ phonon instability was intentionally suppressed by using a coarse energy sampling [22,32]. This comparison thus suggests that the experimentally observed soft-phonon mode is directly related to this $E_{g,1}$ phonon instability, since it is not observed in the calculation of the stable tetragonal structure.

G. Diverging uniaxial phonon Grüneisen parameters

Additional information about this soft-phonon mode can be obtained by examining the thermal-expansion coefficients and their associated uniaxial Grüneisen parameters. As shown in Fig. 7, the low-temperature thermal expansion for $x = 0.10$ is quite anomalous. Here, in a plot of α/T vs T a clear maximum and a minimum at around 10 K are observed along the $[100]_{\text{tet}}$ and $[001]_{\text{tet}}$ directions, respectively. An extrapolation of these curves to $T = 0$ K yields values of α/T near zero (dashed lines in Fig. 7), which excludes an electronic origin related to the pressure dependence of the Sommerfeld coefficient. This is also consistent with the extremely small anomaly at T_c in $[001]_{\text{tet}}$, since this is a purely electronic effect. This maximum (minimum) is clearly closely related to the larger T^3 term of the heat capacity, since no such anomalies are observed in the triclinic phase [see Fig. 1(b)]. Now assuming that we have both the phonon thermal expansion and heat capacity, we can calculate the uniaxial phonon Grüneisen parameters. The dimensionless volume Grüneisen parameter, $\Gamma^{\text{Grüneisen}} = -\partial(\ln\omega)/\partial(\ln V) = (3B_T\alpha)/C_V$, provides information about how the phonon frequencies, ω, respond to volume changes. Here, B_T is the bulk modulus. Without detailed information about the elastic constants, we here simply consider the ratio $\alpha_i/C_{\text{phonon}}$ in Fig. 7(b). This is expected to provide at least a good approximation of the

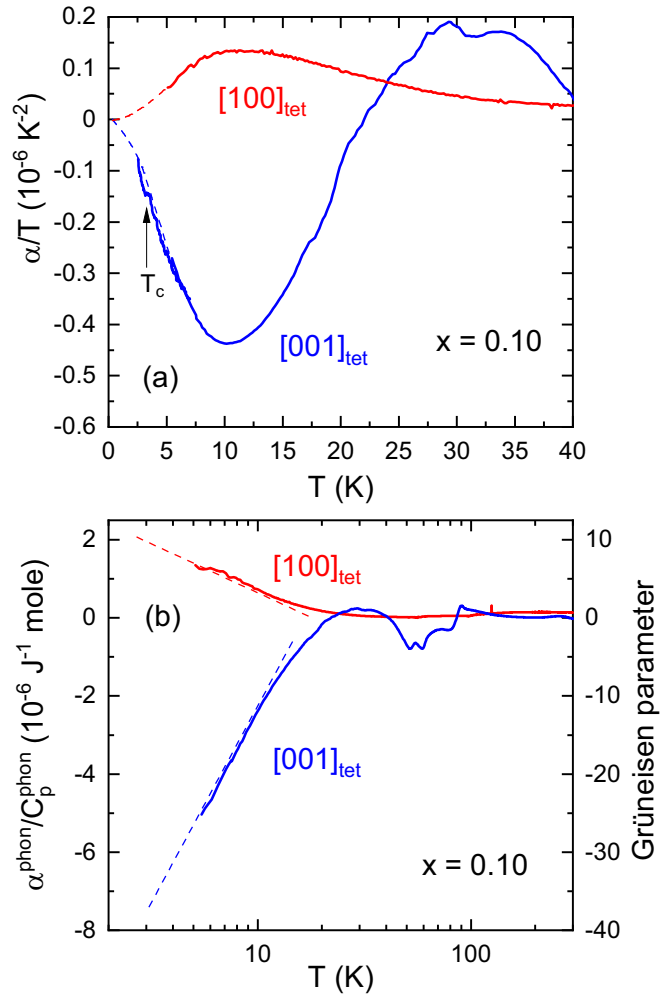

FIG. 7. (a) Maxima and minima in $\alpha_{[100]}/T$ and $\alpha_{[001]}/T$ near 10 K for $x = 0.10$. The dashed lines represent extrapolations to $T = 0$ K, suggesting that electronic effects, due to the pressure dependence of the Sommerfeld coefficient, are small. The superconductivity-induced anomaly at T_c is barely visible along $[001]_{\text{tet}}$. (b) Phonon uniaxial Grüneisen parameters, $(\alpha/C_p)^{\text{phon}}$, highlighting a logarithmic increase down to low T. The values of $\Gamma^{\text{Grüneisen}}$ on the right vertical scale were estimated assuming a "normal" value of 1.5 at room temperature (see text for details).

temperature dependence of the uniaxial Grüneisen parameter $\Gamma_i^{\text{Grüneisen}} \sim \alpha_i/C_p$ under the assumption that the elastic constants vary only weakly with temperature [33]. The behavior of $\Gamma_i^{\text{Grüneisen}}$ is quite novel. At low temperature $\Gamma_i^{\text{Grüneisen}}$ along both $[100]_{\text{tet}}$ and $[001]_{\text{tet}}$ directions exhibits a logarithmic divergence down to the lowest temperature measured, as indicated by the dashed lines. The opposite sign of this divergence along the a and c axes indicates a close connection with the c/a ratio. In order to obtain a feeling for the magnitude of these Grüneisen parameters, we assign a typical $\Gamma^{\text{Grüneisen}}$ value of 1.5 to the volume Grüneisen at 300 K and then obtain the estimated values shown on the right scale of Fig. 7(b). The value of 25 at 5 K along the [001] direction is anomalously enhanced for typical phonon anharmonicity. The logarithmic divergence is suggestive of the proximity to a novel phonon quantum critical behavior. We, however, do not expect the logarithmic divergence to extend to zero temperature, since the transition out of the triclinic phase is first order (see Fig. 4). Quantum critical behavior is often associated with a low-temperature accumulation of entropy, for which a sign change of the thermal expansion under an appropriate tuning parameter is a telltale sign [33]. In our data we see sign changes of the thermal-expansion coefficients both with temperature at T_{cross} [see Figs. 1(b) and 3(b)] and with doping [see Fig. 4(a)]. We are not aware of similar phonon effects in other systems, since quantum criticality is usually associated with electronic degrees of freedom [33,34].

H. Young's modulus: Nematicity?

As mentioned in the Introduction, nematic fluctuations have been associated with the increase in T_c in the closely related $(Ba, Sr)Ni_2As_2$ system [11]. In order to search for nematic signatures in the higher-T_c crystal with $x = 0.10$, Young's modulus, Y, measurements were made using a three-point-bending technique in our capacitance dilatometer [21,35]. We note that Y is, to a good approximation, proportional to the shear modulus near a real nematic transition [21,35], and it is expected to soften significantly at the nematic transition. The temperature dependence of the normalized Y, $Y/Y_{300\,\text{K}}$, are plotted in Fig. 8 along both $[100]_{\text{tet}}$ and $[110]_{\text{tet}}$ directions. Although a significant softening is observed between 50 and 150 K in both sets of data, the data are not compatible with nematic criticality. First, the softening is roughly of equal magnitude along both directions. Second, $Y/Y_{300\,\text{K}}$ is nearly constant below about 50 K. The red dashed curve represents a hypothetical nematic critical curve along $[100]_{\text{tet}}$, i.e., in the B_{1g} channel. The constant values of $Y/Y_{300\,\text{K}}$ are reminiscent of the behavior of the Fe-based materials below the magnetic/nematic transitions [15,21]. The temperature range of the present softening corresponds roughly to the anomalous thermal expansion between T_x and T_{fluct} and not to the temperature of the soft phonon (or anomalous Grüneisen parameters), which happens at much lower temperatures. We note that the lack of a large critical nematic response in $Y/Y_{300\,\text{K}}$ is consistent with elastoresistivity [17] and angle-resolved photoemission spectroscopy data under uniaxial stress [36].

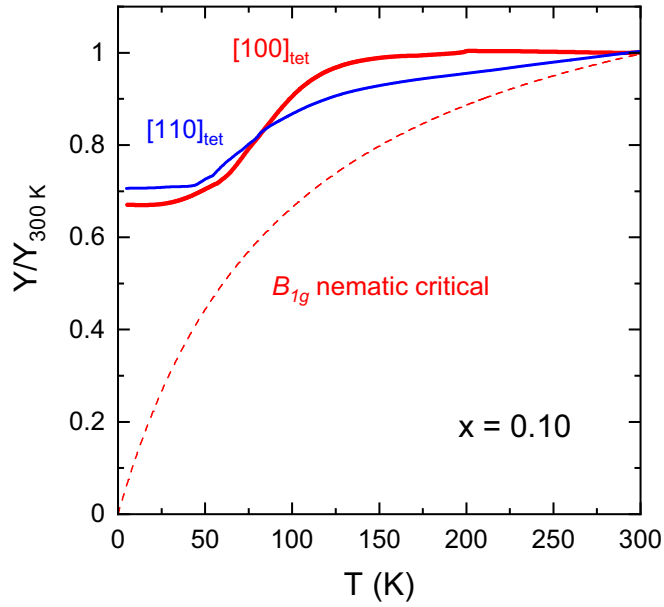

FIG. 8. Normalized Young's modulus, $Y/Y_{300\,\text{K}}$, for a crystal with $x = 0.10$ measured using a three-point-bending technique in a capacitance dilatometer. $Y/Y_{300\,\text{K}}$ softens significantly between 50 and 100 K along both B_{1g} (red) and B_{2g} (blue) directions, but the data are inconsistent with a hypothetical B_{1g} nematic criticality (red dashed line) in which Y vanishes at $T = 0$ K (see text for details).

I. Resistivity scaling for $x = 0.048$ and $x = 0.10$

Finally, we compare the resistivity of the high- and low-T_c crystals in Fig. 9. Here, in order to examine the low-T power-law behavior, we plot the normalized $\rho - \rho_0$ versus temperature on a log-log plot. Interestingly, the resistivity of the higher-T_c crystal ($x = 0.10$) scales like $T^{2.1}$, suggestive of electron-electron scattering. In contrast we find $T^{3.5}$ for

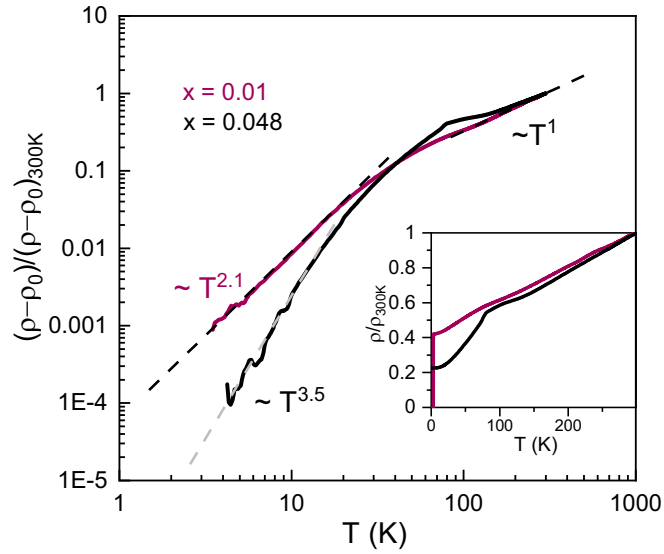

FIG. 9. Low-temperature power-law dependence of the resistivity for $x = 0.048$ and $x = 0.10$. The residual resistivity ρ_0 has been subtracted and the data were then normalized at 300 K. The inset displays $\rho/\rho_{300\,\text{K}}$ versus T.

the low-T_c crystal ($x = 0.048$). Here the exponent is close to the value of 4 expected for electron-phonon scattering in two dimensions at low T, as in graphene [37]. At high temperature, both sets of data roughly approach a linear temperature dependence.

IV. DISCUSSION

The present results provide compelling evidence that the phase diagram of $BaNi_2(As_{1-x}P_x)_2$ is far more interesting and intriguing than suggested by the original data of Kudo *et al.* [10]. We interpret the fourfold symmetry-breaking transition at $T_{\rm orth}$ as the long-range order of the I-CDW [9], and the triclinic phase as a kind of lock-in transition, i.e., C-CDW order. The dominant structural change of the unit cell parameters accompanying these transitions is a large reduction of the c/a ratio in the tetragonal setting, which thus provides an effective tuning parameter in this system. Both the I-CDW and the C-CDW transitions are most likely driven by the same physical mechanism, since c/a evolves in a monotonic fashion upon crossing both transitions.

The I-CDW transition is overshadowed by a large high-temperature fluctuating region, as evidenced by our thermal-expansion data and resulting temperature dependence of the c/a ratio. We note that the onset temperature of these fluctuations, $T_{\rm fluc}$, is roughly coincident with the observation of the $E_{g,1}$ phonon broadening/splitting observed in Raman data [16]. $T_{\rm cross}$, on the other hand, roughly corresponds to the marked increase of the I-CDW peak intensity in x-ray diffraction [9,16]. A weak signal of the I-CDW can in fact already be observed at room temperature [32,38], indicating a very large fluctuation region. The large difference between the onset of the I-CDW signal at $T_{\rm cross}$ and the actual phase transition at $T_{\rm orth}$ again is also consistent with a highly fluctuating order. Near-edge x-ray absorption fine-structure data [9] show that charge/orbital fluctuations exist far above the phase transition and that a temperature-induced charge transfer from $d_{xy,yz}$ to d_{xy} orbitals occurs, which likely is related to the presently observed large changes in c/a. The peak of the B_{1g} elastoresistivity signal occurs at $T_{\rm orth}$, and the signal is mostly confined to the region between $T_{\rm orth}$ and $T_{\rm cross}$ [11,17]. These large fluctuations likely result from the low-dimensional nature of the CDW, which forms quasi-one-dimensional chains of staggered Ni atoms along one of the original [100] tetragonal axes [3,7,9,10]. The here suggested low-dimensional physics is also consistent with the fact that there is very little entropy change associated with the long-range ordering transition at $T_{\rm orth}$ [see Fig. 2(b)]. In this sense, the actual symmetry breaking at $T_{\rm orth}$ can be considered a minor secondary effect.

Since the I-CDW superlattice peaks persist to higher P-substitution levels into the higher-T_c phase, the transition at T_x might constitute a different kind of long-range order of the I-CDW than the orthorhombic structure. More detailed structural investigations are needed to clarify this. Although clearly visible in the thermal-expansion data, this transition appears quite subtle, since no clear signatures have been observed in heat capacity, resistivity, or Raman so far [10,16,17]. Elastoresistivity data exhibit only a broad maximum at 50 K [17], which roughly matches the transition at T_x, although the data do not show any significant hysteresis.

Next we address the increase of the superconducting critical temperature with P substitution. First, we point out that fully P-substituted $BaNi_2As_2$, i.e., $BaNi_2P_2$, is already superconducting with a T_c of roughly 2.5–3 K [39,40], which raises the question of whether fluctuations of the triclinic phase are necessary for producing the higher T_c at $x = 0.10$, or whether it is more appropriate to think of a T_c suppression due to the C-CDW transition and associated triclinic distortion. Although T_c does not change appreciably on going from $x = 0.10$ to $x = 1$, the coupling strength, as quantified by $\Delta C_p/\gamma T_c$ is notably enhanced around $x = 0.10$ ($\Delta C_p/\gamma T_c = 2.0$) from the BCS weak-coupling value of 1.4 (see section on heat capacity and Ref. [10]). A similar enhancement of $\Delta C_p/\gamma T_c$ was also observed in $BaNi_2(P,Ge)_2$ near the onset of a structural distortion or charge density wave, which is also accompanied by a significant phonon softening [41]. An increase in electron-phonon coupling strength, λ, is usually reflected in an increase in $\gamma = N_{\rm bare}(1 + \lambda)$, which is, however, not observed in either of these systems [10,41]. This apparent contradiction can be reconciled by the recent theoretical work using the renormalized Migdal-Eliashberg theory treating electron-phonon coupling close to a CDW instability [42]. The strong anharmonicity of the low-lying phonons, as evidenced by the presently observed extremely large Grüneisen parameters, as well as the extremely low-lying phonon mode [16,31,32], likely contribute to a stronger coupling [43,44]. We note that an enhanced $C_p/\gamma T_c$ value is in contradiction to the theoretical predictions of nematic-mediated superconductivity, which predict a reduction of $C_p/\gamma T_c$ below 1.4 due to a developing gap anisotropy [45]. We note that heat-capacity data on $(Ba,Sr)Ni_2As_2$ find $C_p/\gamma T_c$ roughly equal to 1.4 [11], which is lower than the values in both the P- and Ge-substituted systems. This thus suggests that nematic fluctuations are probably not the main drivers for superconductivity in $BaNi_2(As_{1-x}P_x)_2$ and $BaNi_2(P,Ge)_2$, and that the strong-coupling superconductivity in these systems is most likely related to the soft-phonon modes of the CDW transitions, as originally proposed by Kudo *et al.* [10].

V. CONCLUSIONS

In conclusion, we have demonstrated that the phase diagram of $BaNi_2(As_{1-x}P_x)_2$ is much richer than suggested by the original data of Kudo *et al.* [10], hosting a variety of structural phase transitions related to charge/orbital ordering. Significant precursors above the I-CDW and C-CDW transitions are seen in the anisotropic thermal expansion and c/a ratio of the crystal structure, pointing to low dimensionality and large fluctuations of the charge/orbital ordering. The higher-T_c material is characterized by an additional phase transition to a hitherto unknown structure and by an extremely anharmonic phonon mode, which is likely related to the very broad low-lying $E_{g,1}$ mode observed by Raman [16] and inelastic x-ray studies [31,32]. Associated with this mode is a small Debye-like contribution to the heat capacity and unusually large and diverging Grüneisen parameters, pointing to a possible novel phonon quantum criticality. Finally,

it would be very interesting to perform similar thermal-expansion and shear-modulus measurements on the closely related (Ba,Sr)Ni_2As_2 system, in which the increase of T_c has been attributed to electronic nematicity [11].

ACKNOWLEDGMENTS

We thank Y. Song, M. Yi, and R. Birgeneau for enlightening discussion. Work at KIT was partially funded by the Deutsche Forschungsgemeinschaft (DFG, German Research Foundation) TRR 288-422213477 (Projects A02 and B03). A.S. acknowledges funding from the European Union's Horizon 2020 research and innovation program under the Marie Skłdowska-Curie Grant Agreement No. 847471 (QUSTEC). M.F. acknowledges funding from the Alexander von Humboldt Foundation. K.W. acknowledges funding from the Swiss National Science Foundation through the Postdoc mobility program.

[1] M. Pfisterer and G. Nagorsen, Z. Naturforsch. B **35**, 703 (1980).
[2] F. Ronning, N. Kurita, E. D. Bauer, B. L. Scott, T. Park, T. Klimczuk, R. Movshovich, and J. D. Thompson, J. Phys.: Condens. Matter **20**, 342203 (2008).
[3] A. S. Sefat, M. A. McGuire, R. Jin, B. C. Sales, D. Mandrus, F. Ronning, E. D. Bauer, and Y. Mozharivskyj, Phys. Rev. B **79**, 094508 (2009).
[4] K. Kothapalli, F. Ronning, E. D. Bauer, A. J. Schultz, and H. Nakotte, J. Phys.: Conf. Ser. **251**, 012010 (2010).
[5] B. Zhou, M. Xu, Y. Zhang, G. Xu, C. He, L. X. Yang, F. Chen, B. P. Xie, X.-Y. Cui, M. Arita, K. Shimada, H. Namatame, M. Taniguchi, X. Dai, and D. L. Feng, Phys. Rev. B **83**, 035110 (2011).
[6] C. Eckberg, L. Wang, H. Hodovanets, H. Kim, D. J. Campbell, P. Zavalij, P. Piccoli, and J. Paglione, Phys. Rev. B **97**, 224505 (2018).
[7] S.-H. Lee, J. S. Goh, and D. Cho, Phys. Rev. Lett. **122**, 106404 (2019).
[8] S. Lee, J. Collini, S. X.-L. Sun, M. Mitrano, X. Guo, C. Eckberg, J. Paglione, E. Fradkin, and P. Abbamonte, Phys. Rev. Lett. **127**, 027602 (2021).
[9] M. Merz, L. Wang, T. Wolf, P. Nagel, C. Meingast, and S. Schuppler, Phys. Rev. B **104**, 184509 (2021).
[10] K. Kudo, M. Takasuga, Y. Okamoto, Z. Hiroi, and M. Nohara, Phys. Rev. Lett. **109**, 097002 (2012).
[11] C. Eckberg, D. J. Campbell, T. Metz, J. Collini, H. Hodovanets, T. Drye, P. Zavalij, M. H. Christensen, R. M. Fernandes, S. Lee, P. Abbamonte, J. W. Lynn, and J. Paglione, Nat. Phys. **16**, 346 (2020).
[12] T. Noda, K. Kudo, M. Takasuga, M. Nohara, T. Sugimoto, D. Ootsuki, M. Kobayashi, K. Horiba, K. Ono, H. Kumigashira, A. Fujimori, N. L. Saini, and T. Mizokawa, J. Phys. Soc. Jpn. **86**, 064708 (2017).
[13] Y. Yamakawa, S. Onari, and H. Kontani, J. Phys. Soc. Jpn. **82**, 094704 (2013).
[14] A. Subedi and D. J. Singh, Phys. Rev. B **78**, 132511 (2008).
[15] A. E. Böhmer, T. Arai, F. Hardy, T. Hattori, T. Iye, T. Wolf, H. V. Löhneysen, K. Ishida, and C. Meingast, Phys. Rev. Lett. **114**, 027001 (2015).
[16] Y. Yao, R. Willa, T. Lacmann, S.-M. Souliou, M. Frachet, K. Willa, M. Merz, F. Weber, C. Meingast, R. Heid, A.-A. Haghighirad, J. Schmalian, and M. Le Tacon, Nat. Commun. **13**, 4535 (2022).
[17] M. Frachet, P. W. Wiecki, T. Lacmann, S. M. Souliou, K. Willa, C. Meingast, M. Merz, A. A. Haghighirad, M. Le Tacon, and A. E. Böhmer, arXiv:2207.02462.
[18] G. M. Sheldrick, Acta Crystallogr. A: Found. Crystallogr. **64**, 112 (2008).
[19] V. Petříček, M. Dušek, and L. Palatinus, Z. Kristallogr. - Cryst. Mater. **229**, 345 (2014).
[20] C. Meingast, B. Blank, H. Bürkle, B. Obst, T. Wolf, H. Wühl, V. Selvamanickam, and K. Salama, Phys. Rev. B **41**, 11299 (1990).
[21] A. E. Böhmer, P. Burger, F. Hardy, T. Wolf, P. Schweiss, R. Fromknecht, M. Reinecker, W. Schranz, and C. Meingast, Phys. Rev. Lett. **112**, 047001 (2014).
[22] A. R. Pokharel, V. Grigorev, A. Mejas, T. Dong, A. A. Haghighirad, R. Heid, Y. Yao, M. Merz, M. Le Tacon, and J. Demsar, Commun. Phys. **5**, 141 (2022).
[23] C. Meingast, F. Hardy, R. Heid, P. Adelmann, A. Böhmer, P. Burger, D. Ernst, R. Fromknecht, P. Schweiss, and T. Wolf, Phys. Rev. Lett. **108**, 177004 (2012).
[24] L. Wang, M. He, D. D. Scherer, F. Hardy, P. Schweiss, T. Wolf, M. Merz, B. M. Andersen, and C. Meingast, J. Phys. Soc. Jpn. **88**, 104710 (2019).
[25] A. E. Böhmer, F. Hardy, L. Wang, T. Wolf, P. Schweiss, and C. Meingast, Nat. Commun. **6**, 7911 (2015).
[26] L. Wang, F. Hardy, A. E. Böhmer, T. Wolf, P. Schweiss, and C. Meingast, Phys. Rev. B **93**, 014514 (2016).
[27] M. Rotter, M. Tegel, D. Johrendt, I. Schellenberg, W. Hermes, and R. Pöttgen, Phys. Rev. B **78**, 020503(R) (2008).
[28] J.-H. Chu, J. G. Analytis, C. Kucharczyk, and I. R. Fisher, Phys. Rev. B **79**, 014506 (2009).
[29] L. J. De Jongh and A. R. Miedema, Adv. Phys. **50**, 947 (2001).
[30] Y. Yamamura, A. Horikoshi, S. Yasuzuka, H. Saitoh, and K. Saito, Dalton Trans. **40**, 2242 (2011).
[31] Y. Song, S. Wu, X. Chen, Y. He, H. Uchiyama, B. Li, S. Cao, J. Guo, G. Cao, and R. Birgeneau, arXiv:2207.03289.
[32] S. M. Souliou, T. Lacmann, R. Heid, C. Meingast, L. Paolasini, A. A. Haghighirad, M. Merz, A. Bosak, and M. Le Tacon, arXiv:2207.07191.
[33] M. Garst and A. Rosch, Phys. Rev. B **72**, 205129 (2005).
[34] S. Sachdev and B. Keimer, Phys. Today **64** (2), 29 (2011).
[35] L. Wang, M. He, F. Hardy, P. Adelmann, T. Wolf, M. Merz, P. Schweiss, and C. Meingast, Phys. Rev. B **97**, 224518 (2018).
[36] Y. Guo, M. Klemm, J. S. Oh, Y. Xie, B.-H. Lei, S. Gorovikov, T. Pedersen, M. Michiardi, S. Zhdanovich, A. Damascelli, J. Denlinger, M. Hashimoto, D. Lu, S.-K. Mo, R. G. Moore, R. J. Birgeneau, D. J. Singh, P. Dai, and M. Yi, arXiv:2205.14339.
[37] D. K. Efetov and P. Kim, Phys. Rev. Lett. **105**, 256805 (2010).
[38] M. Merz (private communication).
[39] D. Johrendt, C. Felser, O. Jepsen, O. K. Andersen, A. Mewis, and J. Rouxel, J. Solid State Chem. **130**, 254 (1997).

[40] T. Mine, H. Yanagi, T. Kamiya, Y. Kamihara, M. Hirano, and H. Hosono, Solid State Commun. **147**, 111 (2008).
[41] D. Hirai, F. von Rohr, and R. J. Cava, Phys. Rev. B **86**, 100505(R) (2012).
[42] B. Nosarzewski, M. Schüler, and T. P. Devereaux, Phys. Rev. B **103**, 024520 (2021).
[43] C. Setty, M. Baggioli, and A. Zaccone, Phys. Rev. B **102**, 174506 (2020).
[44] M. Baggioli and A. Zaccone, Phys. Rev. Lett. **122**, 145501 (2019.
[45] S. Lederer, E. Berg, and E.-A. Kim, Phys. Rev. Res. **2**, 023122 (2020).